# MetaScatter: Enabling High-Order Underwater Backscatter via Piezoelectric Metasurface

Juan He[14], Jie Xiong[2], Wenhao Liu[1], Xuan Wang[1], Xiaoyan Wang[1]
Na Chen[1], Chen Liu[1], Chunlong Fei[3], Chao Feng[145*], Xiaojiang Chen[145]
[1]Northwest University, [2] Nanyang Technological University, [3] Xidian University
[4] Shaanxi Key Laboratory of Passive Internet of Things and Neural Computing
[5]Shaanxi International Joint Research Centre for the Battery-Free Internet of Things
Email: {hejuan, liuwenhao, xwang, xywang, chenna}@stumail.nwu.edu.cn, {clfei}@xidian.edu.cn
{liuchen, chaofeng, xjchen}@nwu.edu.cn, jie.xiong@ntu.edu.sg

## Abstract

Underwater communication has long been constrained by the fundamental requirement for low power consumption, driven by applications such as environmental monitoring that demand long-term operation. While backscatter technology is promising in terms of power consumption, existing systems rely on simplistic reflection states (e.g., binary modulation), resulting in low data rates and the communication range is also limited. In this paper, we present MetaScatter, the first piezoelectric metasurface that overcomes these limitations by simultaneously enabling high-order backscatter modulation and beamforming. Unlike conventional mechanical metasurface designs, MetaScatter leverages programmable piezoelectric meta-atoms to control the phase of reflected acoustic signals in real time at milliwatt-level power. By decoupling beamforming and modulation via novel metasurface codebook designs, we achieve long-range communication and high-order modulation with significantly reduced complexity. Experimental results in real-world underwater environments show that MetaScatter supports reliable high-order modulation, including 16-QAM, achieving over 500% higher throughput than the state-of-the-art underwater backscatter system [24].

## CCS Concepts

• **Hardware** → **Wireless devices**; • **Networks** → *Programming interfaces.*

* Corresponding author.


*MobiCom '26, Austin, TX, USA*

ACM ISBN 979-8-4007-2505-0/26/10
https://doi.org/10.1145/3795866.3796677

## Keywords

Underwater Communication, High-order Backscatter, Piezoelectric Metasurface

**ACM Reference Format:**
Juan He[14], Jie Xiong[2], Wenhao Liu[1], Xuan Wang[1], Xiaoyan Wang[1] and Na Chen[1], Chen Liu[1], Chunlong Fei[3], Chao Feng[145*], Xiaojiang Chen[145]. 2026. MetaScatter: Enabling High-Order Underwater Backscatter via Piezoelectric Metasurface. In *The 32nd Annual International Conference on Mobile Computing and Networking (MobiCom '26), October 26–30, 2026, Austin, TX, USA.* ACM, New York, NY, USA, 15 pages. https://doi.org/10.1145/3795866.3796677

## 1 Introduction

Underwater communication plays a crucial role in a variety of applications, including subsea infrastructure inspection and monitoring [30, 36], as well as environmental and ecological assessment [37]. These applications demand long-term monitoring, making energy-efficient communication systems essential for sustaining underwater operations over months or even years without frequent maintenance. To achieve this objective, researchers have explored techniques such as duty cycling [6], adaptive power control [26], and reduced communication rates [26] to extend battery life. Nevertheless, these approaches still struggle with relatively high energy consumption. This is because they rely on active signal transmissions, which requires oscillators and amplifiers to generate and amplify signals. These components consume substantial power, shortening the operational lifespan of battery-powered underwater devices.

To overcome this issue, researchers are turning to backscatter communication technology. Unlike active transmission, backscatter devices communicate by reflecting ambient signals in the environment and thus, enabling ultra-low power operation. In underwater environments, radio waves attenuate rapidly within meters, and light scatters easily, rendering both unsuitable for long-range communication. In contrast, sound waves propagate efficiently through water, making

them the preferred medium for long-range underwater communication. Consequently, acoustic backscatter emerges as a promising approach for enabling energy-efficient, long-range underwater communication. While promising, current acoustic backscatter systems face a key limitation: they can only transmit simple, low-rate messages due to their reliance on basic binary modulation schemes. This limits their ability to support applications that require high throughput, such as transmitting images of endangered coral reefs or videos of underwater infrastructure.

To enhance throughput in backscatter communication, researchers have explored three primary approaches: increasing the switch (backscatter) rate [41], adopting Orthogonal Frequency-Division Multiplexing (OFDM)-based schemes [13], and employing high-order modulation such as quadrature amplitude modulation (QAM) [38, 47]. However, the first approach increases energy consumption as it requires oscillators to operate at higher frequencies. The second method requires wide bandwidths, which are incompatible with the narrowband acoustic transducers typically used in underwater systems. Furthermore, for long-distance communication, the underwater acoustic channel is usually in the low-frequency range and has limited bandwidth. These constraints render the first two approaches impractical for real-world underwater deployment.

In contrast, high-order backscatter communication [3, 38] increases data rates by encoding more bits per symbol through more reflection states, without requiring additional bandwidth or compromising energy efficiency. This makes it a promising candidate for underwater backscatter communication. However, implementing higher-order acoustic modulation (e.g., 16-QAM) is non-trivial and faces two key challenges. On one hand, acoustic systems lack tunable capacitors [34] or delay lines [11, 20]—components commonly used in RF systems that can fine-tune reflection states. As a result, current state-of-the-art underwater systems rely on discrete switch arrays, limiting them to just four reflection states (QPSK/4-QAM), achieving only 2 bits per symbol [3]. On the other hand, simply increasing the number of reflection states reduces the spacing between symbols, which in turn lowers the signal-to-noise ratio (SNR). This issue is exacerbated by underwater conditions—such as severe multipath interference and large signal attenuation—that degrade SNR even more, ultimately limiting the practical communication range for higher-order modulation schemes.

In this paper, we present **MetaScatter, a low-power metasurface-based underwater backscatter system that achieves higher-order modulation (e.g., 16-QAM) and accordingly high data rate without compromising the communication range.** As shown in Figure 1, MetaScatter utilizes a metasurface combined with a microcontroller as a backscatter tag, where each meta-atom can modulate the

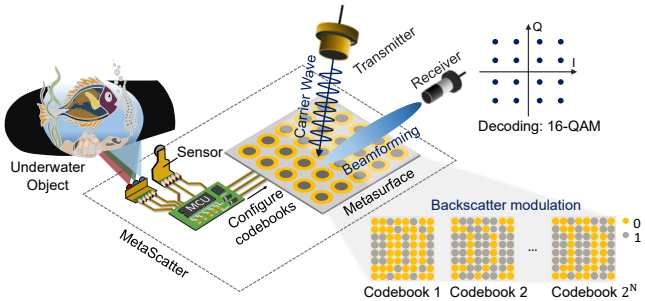


**Figure 1: High-order backscatter communication based on metasurface. A metasurface-based node can enable communication of multiple bits per symbol with high SNR by configuring its codebooks.**

phase of the incident signal. Due to the large number of meta-atoms in a metasurface, a metasurface can generate a wide variety of phase combinations (i.e., codebooks) corresponding to different reflection states, facilitating high-order modulation. Furthermore, the metasurface enables directional beamforming to enhance the reflected signal's SNR and extends the communication range. While promising, realizing such a backscatter system in real life is non-trivial.

First, to enable energy-efficient backscatter communication, we need to design a configurable metasurface capable of dynamically adjusting codebooks in real-time (i.e., within microseconds) to modulate the reflected signal, while operating at ultra-low power—ideally in the milliwatt range. Existing acoustic metasurfaces that rely on mechanical actuators [31, 54, 56] are unsuitable for this purpose, as they consume power at the watt level and suffer from latencies on the order of seconds.

To address this, we electrically modulate the impedance—and consequently the signal phase—using piezoelectric material, rather than altering the signal's propagation path through mechanical structure changes. This is based on a key insight: *the reflection coefficient of piezoelectric materials can be adjusted by tuning their electrical impedance through transient electromechanical coupling* [3]. This enables signal control to be achieved using low-power electrical switching rather than mechanical adjustments. This breakthrough enables microsecond-level phase reconfiguration while consuming only microwatt-level power, effectively overcoming the energy and latency bottlenecks of traditional mechanical approaches. Unfortunately, directly using existing in-air piezoelectric-material-based metasurfaces (PZT-metasurfaces) [40] is ineffective underwater: they exhibit high reflection in air but low reflection in water, resulting in poor signal reflection efficiency. This is because the impedance of water is much higher than that of air, resulting in small impedance difference between the PZT-metasurface and water. Further, the in-air PZT metasurface [40] also fails to achieve effective beamforming underwater. This is due

to the strong coupling between meta-atoms in water, which causes the phase response to deviate from the theoretical design. To address these issues, we first incorporate a structurally optimized passive resonator shell with a closed, air-backed design to increase the impedance contrast, thereby significantly improving reflection efficiency (e.g., > 90%). We then mitigate metasurface coupling by replacing the original resin shell with an aluminum one.

Second, to enable long-range and high-rate communication, it is essential to identify codebooks that can simultaneously achieve high-order modulation (i.e., more reflection states) while preserving beamforming capability. However, the optimal codebooks for these two objectives differ. One possible approach is to exhaustively search all codebooks; however, for an $M \times N$ metasurface, the search space grows exponentially to $2^{M \times N}$, rendering brute-force search computationally infeasible. To address this challenge, we propose an algorithm that decouples the two objectives. We begin by identifying codebooks that enable beamforming by adjusting the phase differences among the meta-atoms. Then, by adding the same phase value (e.g., $\Delta\varphi$) to all the meta-atoms, we preserve the relative phase differences—and thus the beamforming pattern—while altering the absolute phase of the superposed reflected signal. Varying $\Delta\varphi$ yields multiple codebooks with similar beamforming patterns but different signal phases. This approach is grounded in a key observation: beamforming power (i.e., signal amplitude) is governed by the relative phase differences among metasurface meta-atoms, whereas the phase of the reflected signal is determined by their absolute phases. Based on this observation, we can identify codebooks that enable high-order modulation and beamforming simultaneously.

In addition to technical challenges, we also encounter practical ones. Unlike RF metasurfaces, whose structures closely resemble microstrip patches or other planar microwave circuits—allowing direct adoption of mature PCB, LTCC, or thin-film fabrication processes—piezoelectric acoustic metasurfaces lack standardized manufacturing procedures. This challenge is further compounded by underwater operation, which requires waterproofing without compromising performance. To address these challenges, we propose a fabrication workflow that tackles several key issues: (i) minimizing mechanical misalignment and fabrication errors to ensure consistency across meta-atoms; (ii) achieving robust waterproofing without compromising the reflection efficiency or phase response of individual meta-atoms; and (iii) selecting suitable resonator cavity materials to prevent inter-meta-atom coupling, thereby preserving high beamforming gain.

We implemented a prototype of MetaScatter. The end-to-end system comprises a reader with a transmitter and an 8-element hydrophone receiver array, along with a metasurface-based tag containing $14 \times 14$ meta-atoms. An MSP430-based

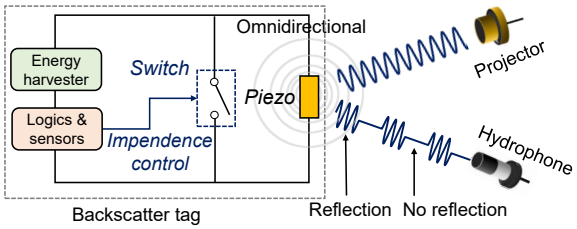


**Figure 2: Principle of underwater acoustic backscatter.**

low-power control module configures the metasurface and modulates the backscatter signal in real time within 50 µs. To mitigate inter-symbol interference (ISI) arising from time-varying multipath induced by water waves, we adopt a multichannel adaptive decision-feedback equalizer (DFE) for robust decoding.

Comprehensive experiments show that the proposed backscatter system supports high-order modulation schemes, achieving reliable communication with QPSK, 8-QAM, and 16-QAM over round-trip ranges of 60 m, 40 m, and 20 m underwater, respectively. Compared to the state-of-the-art underwater backscatter system [24], which is limited to 3 kbps at 10 m, MetaScatter increases throughput by over 500%.

**Contributions:** We present MetaScatter, the first underwater acoustic backscatter system supporting long-range, high-order modulation via a programmable piezoelectric metasurface. By exploiting the electromechanical coupling of piezoelectric materials, we tune their electrical impedance to adjust acoustic impedance, enabling microsecond-level phase control of the metasurface at milliwatt power. To simultaneously achieve high-order modulation and long-range communication, we decouple beamforming, which depends on relative phase differences, from modulation, which relies on the absolute phase of the superposed signal. This decoupling reduces the codebook search complexity from exponential to linear, enabling real-time operation.

## 2 Background on Underwater Backscatter

A typical underwater backscatter link comprises a projector, a hydrophone receiver, and a passive piezoelectric tag, as shown in Figure 2. The projector emits an acoustic carrier that impinges on the tag. By switching an electronic load (e.g., a transistor) across the piezoelectric transducer, the tag modulates its reflection coefficient, imprinting information onto the backscattered wave. The hydrophone captures these modulated reflections and decodes them.

Most existing underwater backscatter systems [2, 5, 24, 35] adopt *binary* modulation (e.g., two reflection states corresponding to "0/1") because it is simple and energy-efficient. However, binary schemes limit the end-to-end throughput. This motivates us to design a system that realizes richer reflection states, which in turn enable higher-order modulations and thereby boost throughput.

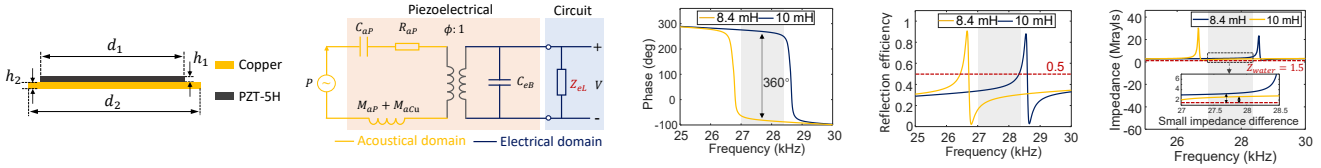


(a) Basic structure. (b) Equivalent circuit. (c) Phase shift. (d) Reflection efficiency. (e) Acoustic impedance.

**Figure 3: Basic copper-backed piezoelectric design.**

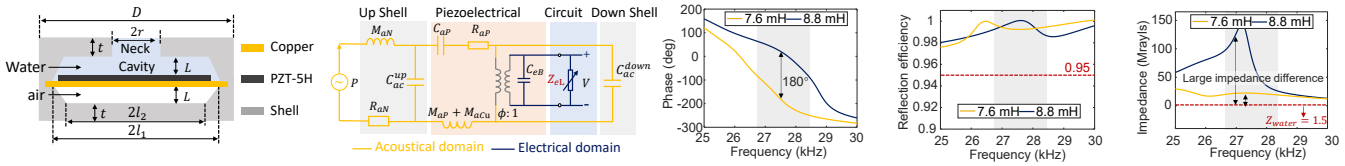


(a) MetaScatter's structure. (b) MetaScatter's Equivalent circuit. (c) Phase shift. (d) Reflection efficiency. (e) Acoustic impedance.

**Figure 4: MetaScatter's meta-atom design.**

## 3 Metasurface Design

This section presents our metasurface design goals, phase-shifting meta-atom design with high reflection efficiency, and underwater-ready assembly.

### 3.1 Design Goals

To achieve a high-rate backscatter communication system, we have the following design goals for the metasurface design: *(1) Real-Time Reconfigurability.* The metasurface must dynamically adjust its properties in real-time (e.g., within μs) to modulate the reflected signal phase, supporting high-rate backscatter communication. *(2) High Reflection Coefficient.* Each meta-atom must exhibit high reflection efficiency to ensure a high SNR. *(3) Low Power Consumption.* For long-term operation, the metasurface must consume minimal power, ideally within the milliwatt ($mW$) range.

### 3.2 Meta-atom Design

*3.2.1 Designing Meta-atom with Phase Shifting Capability.* To realize acoustic meta-atoms with configurable phase-shifting, prior works mainly employed mechanical structures [31, 54, 56], where phase control is achieved by physically altering the propagation path of the meta-atom. While effective, this approach is fundamentally limited in speed and energy efficiency, as it typically relies on stepper motors that are inherently slow and power-hungry.

To overcome these limitations, we use a piezoelectric-material-based structure instead of a mechanically tuned one. Their intrinsic electromechanical coupling enables reflection properties to be jointly determined by material characteristics (e.g., density) and the external electrical load impedance. By adjusting the load impedance, both vibration amplitude and phase can be modulated, enabling real-time meta-atom reconfiguration. Based on this principle, we design a copper-backed piezoelectric meta-atom (Figure 3a). This simple two-layer structure—comprising a circular piezoelectric plate (diameter $d_1$, thickness $h_1$) atop a circular copper sheet (diameter $d_2$, thickness $h_2$)—facilitates fabrication and integration while ensuring effective phase control.

When an acoustic wave impinges on the meta-atom, the reflected signal is characterized by the complex reflection coefficient Γ. Γ describes how much of a wave is reflected by the impedance discontinuity between the transmission medium (i.e., water vs. meta-atom surface). Mathematically, it can be expressed as:

$$\Gamma = \frac{Z_{aMeta} - Z_{water}}{Z_{aMeta} + Z_{water}}, \tag{1}$$

where $Z_{aMeta}$ is the acoustic impedance of the meta-atom, and $Z_{water} = \rho_{water} c_{water}$ is the acoustic impedance of water, with $\rho_{water} = 1000\ kg/m^3$ and $c_{water} = 1500\ m/s$.

Since $Z_{water}$ is constant, controlling the reflection coefficient requires modifying the acoustic impedance of the meta-atom. To this end, we establish an equivalent circuit model of the basic meta-atom, as shown in Figure 3b. The lumped elements represent its electrical properties (static capacitance $C_{eB}$), acoustic vibration properties (copper mass $M_{aCu}$, piezoelectric-plate mass $M_{aP}$, equivalent stiffness $C_{aP}$, and mechanical loss $R_{aP}$), and piezoelectric coupling properties (transformer ratio $\phi$). By connecting an external electrical load $Z_{eL}$, the piezoelectric transformer converts impedance between the acoustic and electrical domains, producing an equivalent acoustic impedance $Z_{aL} = \phi^2 Z_{eL}$. The overall acoustic impedance of the meta-atom $Z_{aMeta}$ can then be derived as:

$$Z_{aMeta} = R_{aP} + i\omega(M_{aP} + M_{aCu}) + \frac{1}{i\omega C_{aP}} + \frac{\phi^2 Z_{eL}}{1 + i\omega C_{eB} Z_{eL}}, \tag{2}$$

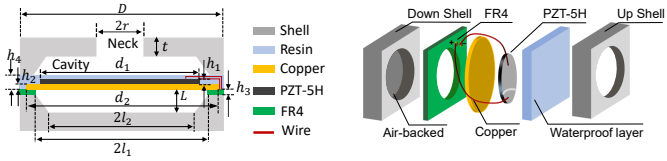


(a) Side view (b) Exploded view

**Figure 5: Design of fabricable meta-atoms.**

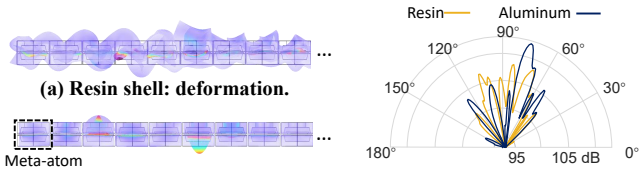


(a) Resin shell: deformation. (b) Aluminum shell: no deformation. (c) Beam pattern.

**Figure 6: Impact of different shell materials.**

where $\omega = 2\pi f_r$, and $f_r$ is the resonant frequency of the structure. The parameters are defined as $M_{aCu} = \frac{4\rho_{cu}h_2}{\pi {d_2}^2}$, $M_{aP} = \frac{4\rho_p h_1}{\pi {d_1}^2}$, $C_{aP} = \frac{S^E h_1}{\pi {d_1}^2}$, and $R_{aP} = 2\xi\sqrt{\frac{M_{aCu}+M_{aP}}{C_{aP}}}$, where $\xi$ is the damping factor, $\rho_{\text{cu}}$ and $\rho_p$ are the densities of copper and PZT-5H, respectively.

From Equation (2), the acoustic impedance of the meta-atom is determined by three factors: geometry (e.g., diameters $d_1$ and $d_2$, thicknesses $h_1$ and $h_2$), material properties (e.g., densities $\rho_p$ and $\rho_{cu}$ of the piezoelectric and copper plates, and piezoelectric elastic compliance constant $s^E$), and the external electrical load $Z_{eL}$. Once fabricated, the geometry and material properties are fixed and immutable. In contrast, through electromechanical coupling, the acoustic impedance can be dynamically tuned by adjusting the external electrical load $Z_{eL}$. This tuning directly controls the reflection coefficient $\Gamma$ and the signal phase.

To validate this principle, we use COMSOL [1], a finite-element multiphysics simulator, to analyze the phase shift across different frequencies under varying inductances. Specifically, changing the inductor $L_{eL}$ modifies the electrical load impedance as $Z_{eL} = i\omega L_{eL}$. As shown in Figure 3c, the results confirm that adjusting $L_{eL}$ produces a full $2\pi$ phase shift, verifying the feasibility of impedance-based phase control.

**Low-power 1-bit Phase Shift Design.** We adopt a 1-bit phase design despite the theoretical continuous $0$–$2\pi$ tuning requirement. Continuous-tuning components commonly used in RF metasurfaces (e.g., varactor diodes and tunable inductors) are acoustically incompatible, as their tunable inductance and capacitance are orders of magnitude smaller than the values required for acoustic metasurfaces. While multi-state control circuits could be employed, they significantly increase complexity and power consumption. Instead, we implement a simple solution that toggles between two inductors via a low-power switch, enabling reliable $0/\pi$ phase control with minimal hardware and energy overhead.

*3.2.2 Designing Meta-atom with High Reflection Efficiency.* Although the basic copper-backed piezoelectric structure enables phase control, it suffers from low reflection efficiency ($\leq$ 50%) in the target frequency range when operated in underwater environments, as shown in Figure 3d. This limitation arises from a small acoustic impedance difference between water and the meta-atom (Figure 3e), resulting in reduced reflection of the incident acoustic power.

To overcome this limitation, we introduce a passive shell to increase the effective acoustic impedance of the meta-atom. By coupling the piezoelectric element with a high-impedance shell in series, the overall impedance difference between water and the meta-atom is enlarged, improving reflection efficiency. The structure and its lumped-element equivalent circuit are shown in Figure 4a and Figure 4b. The total acoustic impedance of the new design is:

$$Z^*_{aMeta} = R_{aN} + i\omega M_{aN} + \frac{Z_{aMeta}}{1 + i\omega C_{aC} Z_{aMeta}}, \tag{3}$$

where the lumped parameters of the passive shell are defined as follows:

$$\begin{cases} R_{aN} = \left(\frac{t}{r} + 2\right)\sqrt{\frac{2\mu\rho_{\text{water}}\omega}{\pi r^2}} + \frac{\rho_{\text{water}} c_{\text{water}}}{\pi r^2}\left[1 - \frac{2J_1(2kr)}{2kr}\right], \\ M_{aN} = \frac{\rho_{\text{water}}\left[t + 0.85r\left(2 - 0.7\frac{r}{l_1}\right)\right]}{\pi r^2}, \\ C^{\text{up}}_{aC} = \frac{V}{\rho_{\text{water}} c^2_{\text{water}}}, \qquad C^{\text{down}}_{aC} = \frac{V}{\rho_{\text{air}} c^2_{\text{air}}}. \end{cases} \tag{4}$$

The air density and the sound speed are $\rho_{air}$ and $c_{air}$, respectively. The parameter $J_1$ is the Bessel function of the first kind, and $\mu$ is the dynamic viscosity coefficient. The parameter $V$ is the cavity volume, while $t$, $r$, and $l_1$ are geometric parameters as illustrated in Figure 4a. We have $k = 2\pi f_r^{new}/c_{water}$, where $f_r^{new}$ is the resonant frequency of the new structure. This resonant frequency is determined by both the shell and the basic copper-backed piezoelectric structure.

Equations (3) and (4) highlight that the effective acoustic impedance depends on both the shell geometry and the underlying piezo structure $Z_{aMeta}$. Thus, we carefully tune the shell's geometric parameters while adjusting the electrical load of the piezo to preserve the 180° phase shift. The geometry is optimized through enumeration in COMSOL. Results (Figure 4c– 4d) confirm that the optimized meta-atom achieves both high reflection efficiency ($\geq$ 90%) and 180° phase shift in the working band.

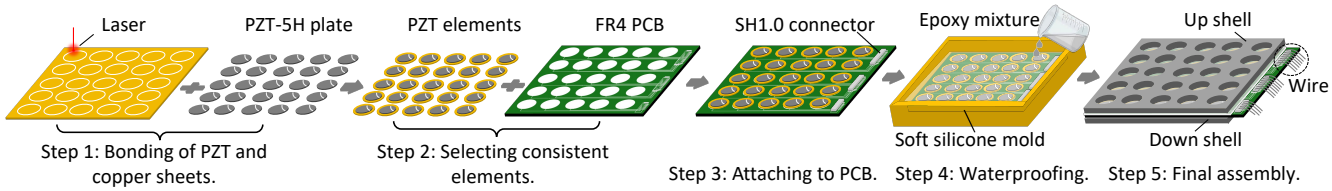


**Figure 7: Workflow of piezoelectric metasurface fabrication.**

## 3.3 Metasurface Assembly

We now detail the integration of the underwater metasurface, beginning with the electrical connection, waterproofing strategy, and shell material selection, followed by a description of the fabrication workflow.

**Electrical Connection.** We use an FR4 substrate to route signals between meta-atoms and the external control circuitry. To minimize the FR4's impact on the intrinsic resonance, a cavity is carved within the substrate (Figure 7). The electrodes of the piezoelectric plates are wire-bonded to FR4 bonding pads, which are then connected to a unified PCB trace layout. This ensures consistent electrical interfacing across the entire metasurface.

**Waterproofing.** Waterproofing is essential to prevent electrode short-circuiting in water. A simple rigid coating is not a viable solution as high-impedance materials reflect sound and suppress modulation. To retain tunability, the coating material must instead have an acoustic impedance close to that of water. Guided by this principle, we select a low-cost GOET-1080 epoxy mixture [10]. The epoxy coating, however, also alters the resonant frequency of the metasurface. To mitigate this effect, we jointly optimize the thickness of the epoxy layer and the FR4 substrate to preserve the desired resonance. In the final design (Figure 5), a 3 mm epoxy layer is used, and we provide the details of the geometry parameters of MetaScatter's structure in Appendix A.

**Shell Material Selection.** Since all meta-atoms are coupled through a common shell (Section 3.2.2), the shell material plays a critical role in determining the overall performance. Materials widely used in air, such as resin or PLA [40], deform significantly underwater (Figure 6a). The resin's low acoustic impedance—stemming from its lower density and sound velocity—causes acoustic energy to leak into the shell. The resulting shell vibrations impose additional forces on the meta-atoms, shifting their resonant frequency and ultimately distorting the reflection phase. Consequently, the metasurface fails to maintain effective beamforming in the target frequency band (Figure 6c). In contrast, metals such as aluminum or steel offer a much larger acoustic impedance difference; we therefore select aluminum as the final shell material. As shown in Figures 6b and 6c, the aluminum shell suppresses structural deformation and enables accurate, high-gain beamforming.

**Fabrication Workflow.** We fabricate a piezoelectric acoustic metasurface following the procedure shown in Figure 7. *Step 1: Bonding the piezoelectric material with the copper sheets.* PZT-5H plates [7] are bonded to copper discs using epoxy adhesive [10]. *Step 2: Selecting consistent elements.* To ensure uniformity, elements are screened using a WK6500B impedance analyzer [50], and only those with resonant frequencies and impedances within 10% of the theoretical values are retained. *Step 3: Attaching to PCB.* The copper-backed PZT elements are bonded onto the FR4 PCB, with electrical connections established through soldering and wire bonding. *Step 4: Waterproofing.* The assembly is encapsulated in a silicone mold and filled with degassed epoxy. To avoid bubble-induced reflections, the epoxy is vacuum degassed, syringe-extracted to remove residual bubbles, and cured for 24 h before CNC polishing (±0.1 mm) to ensure surface flatness. *Step 5: Final assembly.* Upper and lower shells are CNC-machined from aluminum and bonded to the structure with high-strength epoxy. External leads exit via an SH1.0 connector, which is potted with epoxy for waterproof sealing.

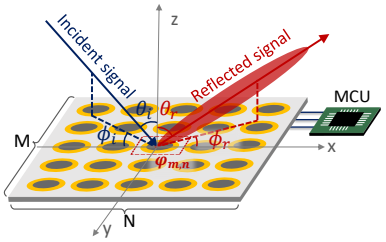


**Figure 8: Metasurface reflection signal model.**

# 4 High-order Backscatter Communication

In this section, we aim to achieve long-range high-order backscatter modulation using metasurfaces. First, we select optimal reflection states to enable high-order modulation with strong SNR, and then present the corresponding decoding pipeline.

## 4.1 High-order Modulation

To enable high-order backscatter modulation, we configure the metasurface's codebook to fine-tune the reflected signal's amplitude and phase. As shown in Figure 8, the reflected signal towards the azimuth angle $\theta_r$ and elevation angle $\phi_r$

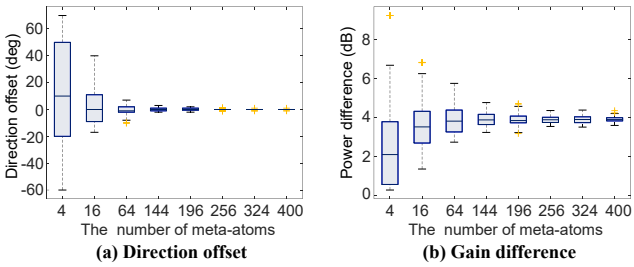


(a) Direction offset (b) Gain difference

**Figure 9: Performance gap between continuous and 1-bit metasurface in terms of beamforming direction accuracy and power gain.**

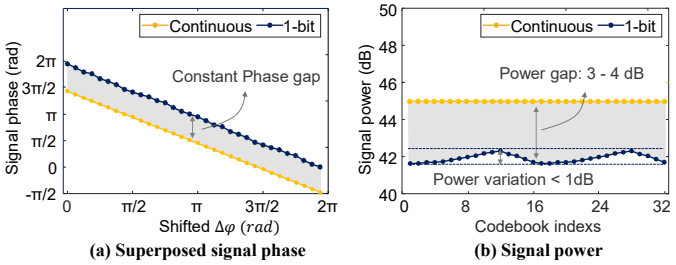


(a) Superposed signal phase (b) Signal power

**Figure 10: Phase modulation performance of a $14 \times 14$ continuous metasurface versus a $14 \times 14$ 1-bit metasurface.**

can be calculated as:

$$R_{\theta_r,\phi_r} = \sum_{m=1}^{M}\sum_{n=1}^{N} \sqrt{\sigma} e^{j\varphi^I_{m,n}(\theta_i,\phi_i)} \cdot e^{j\varphi^C_{m,n}} \cdot e^{j\varphi^R_{m,n}(\theta_r,\phi_r)}, \quad (5)$$

where $\sqrt{\sigma}$ is the amplitude. The term $e^{j\varphi^I_{m,n}(\theta_i,\phi_i)}$ represents the phase delay introduced by the incident wave from direction $(\theta_i, \phi_i)$, and $e^{j\varphi^R_{m,n}(\theta_r,\phi_r)}$ represents the phase delay introduced by the reflected wave. Equation (5) shows that configuring the phase combination of each meta-atom (i.e., codebook $\boldsymbol{\Phi} = \{\varphi^C_{1,1}, \varphi^C_{1,2}, ..., \varphi^C_{m,n}\}$) can alter the reflection state. For example, a $M \times N$ metasurface can yield $2^{M\times N}$ reflection states.

For long-range, high-order modulation (e.g., QAM), codebooks must simultaneously: (1) provide beamforming to amplify signals, and (2) ensure sufficient state separation for symbol discrimination. Achieving both, however, requires precise phase control at each meta-atom, and the optimal codebooks for the two objectives differ. Given the vast search space ($2^{M\times N}$), brute-force enumeration is infeasible. We therefore propose an algorithm that decouples the two objectives, efficiently identifying codebooks by modulating states along the beamforming direction.

*4.1.1 Beamforming.* To realize beamforming, the reflected signals from all meta-atoms must be phase-aligned toward the desired direction. As shown in Figure 8, let the angles of the incident wave and desired reflection be $(\theta_i, \phi_i)$ and $(\theta_r, \phi_r)$, respectively. The phase delay of the incident wave at the $(m,n)^{th}$ meta-atom is:

$$\varphi^I_{m,n} = k\big(md \sin\theta_i \cos\phi_i + nd \sin\theta_i \sin\phi_i\big). \quad (6)$$

To align all paths constructively in the direction $(\theta_r, \phi_r)$, the phase delay of the outgoing reflected wave should be:

$$\varphi^R_{m,n} = k\big(md \sin\theta_r \cos\phi_r + nd \sin\theta_r \sin\phi_r\big). \quad (7)$$

Therefore, the $(m,n)^{th}$ meta-atom must apply a compensation phase of

$$\varphi^C_{m,n} = \varphi^R_{m,n} - \varphi^I_{m,n}, \quad (8)$$

where $k = 2\pi/\lambda$ and $\lambda$ is the wavelength of the incident signal. The set $\boldsymbol{\Phi^C} = \{\varphi^C_{1,1}, \varphi^C_{1,2}, \ldots, \varphi^C_{M,N}\}$ thus constitutes the *beamforming codebook*.

According to Equation 8, the ideal beamforming codebook is a set of continuous phase shifts. However, MetaScatter's metasurface is a 1-bit design with two phase states: 0 and $\pi$. To quantize continuous phase compensation into 1-bit phase states, we use the following rule [15]:

$$Q(\varphi^C_{m,n}) = \begin{cases} 0, & \pi/2 \le \varphi^C_{m,n} < 3\pi/2 \\ \pi, & \text{otherwise.} \end{cases} \quad (9)$$

Phase quantization brings phase error and inevitably degrades the beamforming performance. To investigate this impact, we analyze the performance gap between continuous and 1-bit metasurfaces in terms of power gain and beamforming direction accuracy. Figure 9 shows that as the number of meta-atoms in the metasurface increases, the direction offset decreases and eventually approaches zero. The difference in power gain stabilizes at 3-4 dB. To summarize, even with just a 1-bit state change (i.e., two states), a metasurface with a large number of meta-atoms (e.g., exceeding 144 meta-atoms) can achieve comparable beamforming performance to that achieved with continuous phase shifts.

*4.1.2 Programming the Signal Phase without Compromising its Beamforming Capability.* Next, we aim to design codebooks that enable phase modulation while preserving beamforming gain and direction. To achieve this, our solution is based on two key insights: (1) for a given incident and reflection angle, the overall phase of the reflected signal is determined by the superposition of the absolute phases of individual meta-atoms; and (2) beamforming performance depends only on the relative phase differences between meta-atoms. Thus, after computing the beamforming codebook $\boldsymbol{\Phi^C} = \{\varphi_{1,1}, \varphi_{1,2}, \cdots, \varphi_{M,N}\}$[1], we can add the same phase offset $\Delta\varphi$ to all elements to form a new codebook $\boldsymbol{\Phi^C} + \Delta\varphi = \{\varphi_{1,1} + \Delta\varphi, \ldots, \varphi_{M,N} + \Delta\varphi\}$. This effectively rotates all elements by a phase of $\Delta\varphi$ while keeping their relative phase

[1]The amplitudes of the reflected signals from each meta-atom are similar, and we normalize them to unity for simplicity of representation.

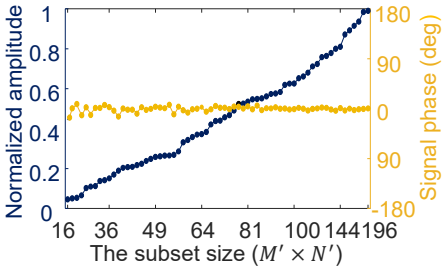


**Figure 11: Amplitude modulation. Configuring the signal amplitude without changing its phase.**

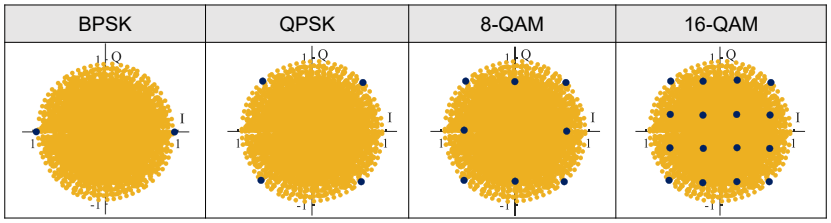


**Figure 12: The constellation diagram of different QAM modulation schemes. The yellow dots represent the full range of phase and amplitude control achievable by 1-bit codebooks generated using our strategy. The dark blue dots represent the selected points to form different n-QAM constellations.**

differences unchanged, thereby maintaining beamforming but shifting the phase of the superposed signal.

However, directly adding $\Delta\varphi$ to a 1-bit codebook results in only two possible phase states (0 and $\pi$), which is insufficient for fine-grained phase modulation. Fortunately, we find that for a metasurface with a sufficiently large number of meta-atoms (e.g., 196 in our design), the superposed signal phase error introduced by quantization exhibits statistical stability. As shown in Figure 10, the resulting superposed phase difference between the ideal continuous codebooks and the 1-bit codebooks remains approximately constant for different shifts $\Delta\varphi$. As a result, we effectively achieve quasi-continuous phase modulation (e.g., 32 phase levels) of the superposed signal while maintaining power variation below 1 dB—despite the hardware limitation of purely 1-bit phase control.

*4.1.3 Programming the Beamforming Signal Amplitude.* We now consider the control of the main-lobe amplitude. Intuitively, for a metasurface with $M \times N$ meta-atoms, the reflected signal reaches its maximum amplitude when all reflection vectors are perfectly aligned. To enable amplitude tuning, our basic idea is to align a subset of meta-atoms (i.e., $M' \times N'$) for beamforming and vary the size of this subset to achieve the desired signal amplitude. We then ensure that the remaining meta-atoms do not interfere with the designed amplitude. Furthermore, the resulting codebooks must preserve the phase-modulation capability described in Section 4.1.2.

We formulate this objective as an optimization problem. Without loss of generality, we assume that the maximum achievable amplitude of an $M \times N$ metasurface is normalized to 1. For the desired amplitude of $\frac{M' \times N'}{M \times N}$, we can select a subset of $M' \times N'$ meta-atoms and calculate their phase states according to the beamforming algorithm. To optimize the phase states of the remaining $MN - M'N'$ meta-atoms, we define our objective function as below:

$$\boldsymbol{\Phi} = \arg\min_{\boldsymbol{\Phi}^*} \left| R^*_{\theta_r,\phi_r} - R_{\theta_r,\phi_r} \right|, \tag{10}$$

where $R^*_{\theta_r,\phi_r}$ (desired amplitude) and $R_{\theta_r,\phi_r}$ (actual amplitude) in direction $(\theta_r, \phi_r)$ are calculated using Equation (5). To ensure our 1-bit codebooks $\{\boldsymbol{\Phi}_1^{1-bit}, \boldsymbol{\Phi}_2^{1-bit}, \cdots, \boldsymbol{\Phi}_Q^{1-bit}\}$ achieves a small main-lobe power variation, we refine the objective function as:

$$\boldsymbol{\Phi} = \arg\min_{\boldsymbol{\Phi}^*} \underbrace{\frac{1}{Q}\sum_{q=1}^{Q} \left| R^*_{\theta_r,\phi_r} - R_{\theta_r,\phi_r}(\Phi_q^{1-bit}) \right|}_{minimize\ the\ gap}, \tag{11}$$

$$\text{s.t.} \quad \underbrace{20log10\frac{\max\{|\boldsymbol{R}_{\boldsymbol{\theta_r},\boldsymbol{\phi_r}}|\}}{\min\{|\boldsymbol{R}_{\boldsymbol{\theta_r},\boldsymbol{\phi_r}}|\}}}_{minimize\ the\ variance} < \delta. \tag{12}$$

where $Q$ represents the desired number of modulation phases, $\delta$ represents the threshold of variation value, and $\boldsymbol{R}_{\boldsymbol{\theta_r},\boldsymbol{\phi_r}} = \{R_{\theta_r,\phi_r}(\Phi_1^{1-bit}), R_{\theta_r,\phi_r}(\Phi_2^{1-bit}), \cdots, R_{\theta_r,\phi_r}(\Phi_Q^{1-bit})\}$ represents the reflection signals of different 1-bit codebooks. This optimization problem can be efficiently solved using Genetic Algorithm [23] or Particle Swarm Optimization [25].

We validate this approach in simulation by varying the subset size up to $14 \times 14$ meta-atoms and generating the corresponding 1-bit codebooks. As shown in Figure 11, the proposed method enables precise main-lobe amplitude tuning while maintaining minimal phase variation.

*4.1.4 Identifying Codebooks for Different Modulation Schemes.* The above strategy generates codebooks with arbitrary beamforming power and phase for given incidence and reflection angles, as illustrated by the yellow points in Figure 12. The next step is to select codebooks from these candidates for specific modulation schemes. To achieve this, we utilize standard QAM constellation $\boldsymbol{R}^{\boldsymbol{ideal}} = \{R_1^{ideal}, \cdots, R_P^{ideal}\}$ as the desired constellation symbols. We then select the codebooks whose corresponding symbols in the I/Q plane lie exactly on the desired constellation points $\boldsymbol{R}^{\boldsymbol{ideal}}$. Formally, if $R(\boldsymbol{\Phi}_q)$ is the complex reflection coefficient of codebook $\boldsymbol{\Phi}_q$, we aim

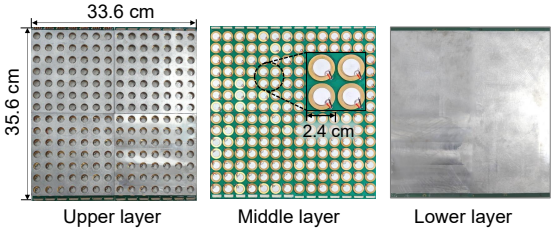


**Figure 13: The prototype of the metasurface.**

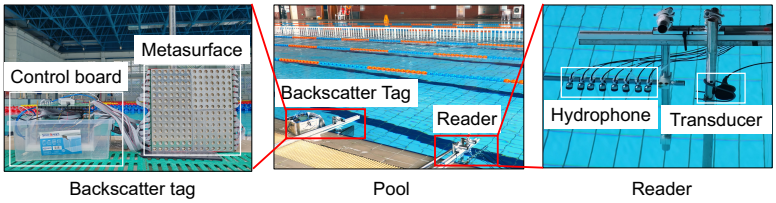


**Figure 14: The system setup.**

to select a codebook set $C = \{\Phi_1, \ldots, \Phi_Q\}$ such that:

$$C^\star = \underset{C}{arg\,min} \left| R_p^{ideal} - R(\Phi_q) \right|. \tag{13}$$

Following these rules, our implementation strategically maps the selected codebooks onto standard QAM constellations, as indicated by the dark-blue points in Figure 12.

## 4.2 Demodulation

In practical underwater environments, the received signal is distorted by noise and multipath, resulting in inter-symbol interference (ISI). To mitigate this, we adopt an adaptive multi-channel decision-feedback equalizer (DFE) [14, 44], which performs per-symbol channel estimation. Each packet consists of a preamble sequence $p_1, \ldots, p_N$ followed by the data payload. The preamble is used to train the adaptive multi-channel DFE. We construct a composite tap vector $\widehat{\mathbf{h}}$ that collects $K$-channel feedforward taps ($K = 8$) and feedback taps. In the preamble, $\widehat{\mathbf{h}}(n)$ is updated at each symbol $n$ using RLS algorithm:

$$\widehat{\mathbf{h}}(n) = \widehat{\mathbf{R}}_{uu}^{-1}(n)\, \widehat{\mathbf{r}}_{ud}(n), \tag{14}$$

where $\widehat{\mathbf{R}}_{uu}(n) = \sum_{m=0}^{n} \lambda^{n-m} \mathbf{u}(m)\mathbf{u}^H(m)$, $\widehat{\mathbf{r}}_{ud}(n) = \sum_{m=0}^{n} \lambda^{n-m} \mathbf{u}(m) p_m^*$, $p_m^*$ denotes the complex conjugate of the decided symbol at symbol time $m$, and $\lambda$ denotes the forgetting factor. The regressor vector $\mathbf{u}(m) = [v_1^T(m) e^{-j\hat{\theta}_1(m)}, \ldots, v_K^T(m) e^{-j\hat{\theta}_K(m)}, -\hat{\mathbf{d}}^T(m)]^T$ contains the phase-corrected sample vectors $\mathbf{v}_k(m)$ (one per hydrophone, after decision-directed PLL rotation $\hat{\theta}_k(m)$) and the previously decided symbols $\hat{\mathbf{d}}(m)$ that are fed back for ISI cancellation. After the preamble ($n = N$), the estimated $\hat{\mathbf{h}}(N)$ is then applied to decode the payload.

**Lessons Learned from Demodulation:** 1) With more channels, we can exploit their spatial diversity to coherently combine multiple arrivals, boosting effective SNR and mitigating fading and ISI. This approach requires no prior knowledge of path angles and works with arbitrary hydrophone array geometries. 2) Higher-order modulation schemes, such as 8-QAM and 16-QAM, require a longer equalizer (i.e., a longer training preamble and more feedforward/feedback taps) to enable accurate decoding. This is because their denser symbol spacing makes them markedly less tolerant to residual ISI and channel distortion.

# 5 Prototype Implementation

## 5.1 Metaurface Implementation

**(a) Metasurface Fabrication.** We fabricated different sizes of piezoelectric acoustic metasurfaces with $7 \times 7$, $7 \times 14$, and $14 \times 14$ meta-atoms. Each meta-atom is designed with a side length of 2.4 cm, resulting in an overall size of 33.6 $cm \times$ 33.6 $cm$ for the $14 \times 14$ metasurface. An SH1.0 wiring connector protrudes an additional 2 $cm$ from one edge of the panel. Figure 13 illustrates the prototype of the $14 \times 14$ metasurface, which consists of three layers. The upper and lower layers are aluminum shells, while the middle layer houses 196 custom copper-backed PZT elements with a transparent waterproof coating. The cost of the metasurface is about \$50, and the control module costs about \$70, bringing the total cost (\$120) to a level comparable to that of a low-cost acoustic modem.

**(b) Hardware Control Module.** To control the metasurface, we custom-designed a control circuit, which consists of an MCU (MSP430G2553 [45]), 49 four-channel switch ICs (TMUX- 1134PWR [46]), and 392 inductors [28]. Each meta-atom is connected to two inductors and one switch channel. To reduce the control overhead, we connect each column of the metasurface to a single GPIO control pin, which requires 14 pins in our implementation. To enable real-time reconfiguration, the GPIO interface is directly connected to supply the bias voltage to the switches, allowing rapid reconfiguration on the microsecond scale due to the short rise/fall times of the GPIO signals and the small time constants of the inductors.

## 5.2 Reader Implementation

MetaScatter can operate with the transmitter and receiver either separated or co-located. In this paper, we focus on the co-located configuration, where both are integrated into a single reader unit comprising two main components:

**(a) Transmitter.** The transmitter serves as the carrier source, continuously emitting a pure-tone carrier. We use a commercial transducer [53] as the projector. A sine wave of the

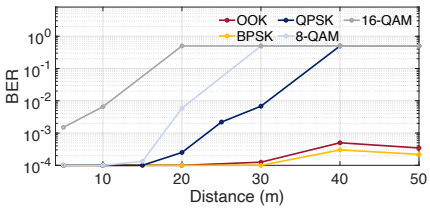


Figure 15: Communication range.

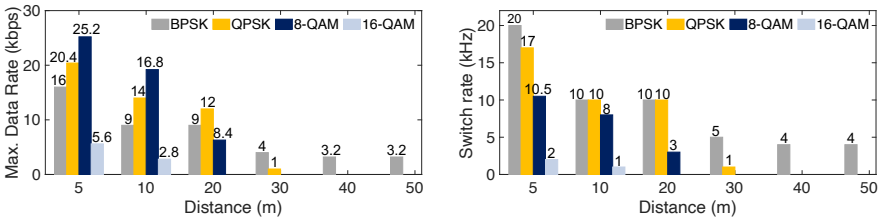


(a) The maximum effective data rate (b) The switch rate

Figure 16: The maximum data rate and the corresponding switch rate.

desired amplitude and frequency is generated by a RIGOL DG1022 arbitrary waveform generator [42] and fed into an Aigtek ATA-214 power amplifier [4], whose output drives the transducer. Due to the transducer's directional nature, self-leakage into the co-located receiver array is minimized.

**(b) Receiver Array.** The backscattered signal is received by an 8-element receiver array shown in Figure 14, which consists of 8 low-cost Aquarian Audio H1a hydrophones [8]. Each H1a hydrophone is connected to a 26 dB PA6 amplifier [9]. The received signal is sampled by ZOOM-F8N PRO [57]. The recorded data are then fed into the decoding pipeline as described in Section 4.2.

## 5.3 Evaluation Setup

**(a) Testing Environment.** The experiments were conducted in a 30 $m \times 50\ m \times 2\ m$ swimming pool (Figure 14). We fixed the equipment on the poolside and used a rigid pole to lower the reader and metasurface to a depth of about 1 m.

**(b) Metrics.** We evaluate performance in terms of effective data rate, bit-error rate (BER), and signal-to-noise ratio (SNR).

**(c) Backscatter Modulation Schemes.** Metascatter supports different modulations—from OOK and BPSK to higher-order modulations such as QPSK, 8-QAM, and 16-QAM. In the overall performance evaluation (Section 6.1), we report their communication range, maximum data rate, BER, and SNR. In other controlled experiments, we use QPSK as the default modulation scheme.

# 6 Evaluation

## 6.1 Overall Performance

**Communication Range.** In this section, we first evaluate the uplink communication range at which we can reliably communicate (i.e., $BER < 10^{-2}$) for different modulation schemes. In this experiment, the backscatter switch rate was fixed at 1000 Hz, while the distance between the backscatter tag and the reader was varied. At each distance, we conducted 5 trials per modulation scheme. Figure 15 plots the median BER versus the communication range. The achievable range decreases for higher-order modulations due to their denser constellation spacing. Nevertheless, even with a 16-QAM modulation scheme, we achieve a round-trip range of 20 m, while 8-QAM and QPSK extend the range to 40 m and 60 m, respectively. For simpler binary modulations (i.e., OOK/BPSK), we can support a round-trip communication range of 100 m at the BER of $3.12 \times 10^{-4}$ and $4.12 \times 10^{-4}$, respectively. According to the recent underwater backscatter link budget theory [5], MetaScatter's uplink communication range can theoretically reach 170 m. These results demonstrate that MetaScatter significantly extends the range of underwater backscatter communication.

**Throughput.** In this experiment, we varied the backscatter switch rate and measured the maximum data rate achieved by the backscatter node while maintaining a bit error rate below $10^{-2}$. Each configuration was repeated five times. Figure 16 reports the achievable data rate and corresponding backscatter switch rate under different modulation orders and distances. At short ranges (5–10 m), higher-order constellations generally yield higher throughput, since each symbol encodes more bits. For example, 8-QAM achieves up to 25.2 kbps at 5 m, outperforming both BPSK and QPSK. However, 16-QAM exhibits a counter-intuitive drop in throughput. This is because higher-order modulations impose stricter SNR requirements on the switch rate: as shown in the right panel, 16-QAM can only sustain 2 kHz at 5 m, compared to 20 kHz for BPSK. The reduced switching capability directly constrains the maximum data rate, making 16-QAM inferior to lower-order modulations in practice.

At 20 m, 8-QAM throughput falls sharply, leaving QPSK as the best performer. At 40 m, only BPSK maintains a usable link, achieving the highest throughput at this range. These results highlight that throughput is jointly determined by modulation order and feasible switch rate: although higher-order modulations theoretically offer higher data rates, their greater SNR sensitivity limits the effective switch rate, resulting in lower throughput than simpler modulations at longer distances.

## 6.2 Benchmark

In this section, we evaluate the effect of each individual design component. We use QPSK modulation schemes as the representative case.

**Random Codebooks vs. Optimized Codebooks.** To quantify the benefit of the codebook optimization introduced in Section 4, we compare the performance of our optimized

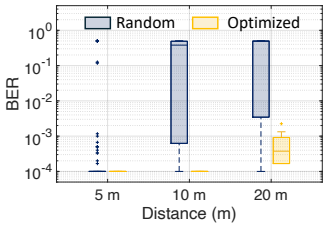


**Figure 17: Random vs. Optimized codebooks.**

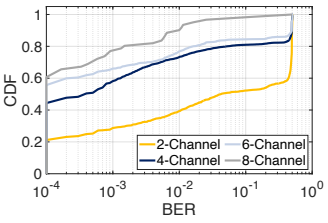


**Figure 18: Impact of hydrophone channels.**

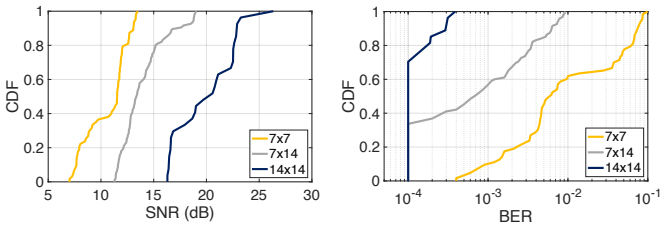


**(a) SNR (dB)** **(b) BER**

**Figure 19: Impact of metasurface size.**

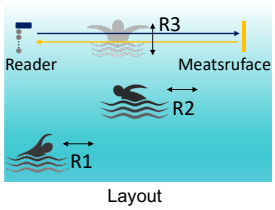


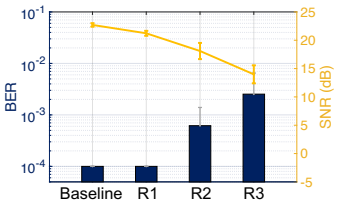


**Figure 20: Dynamic interference.**

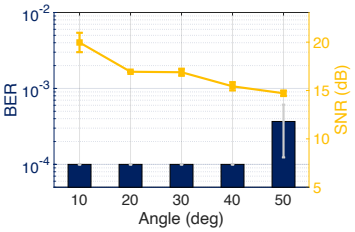


**Figure 21: Impact of angle.**

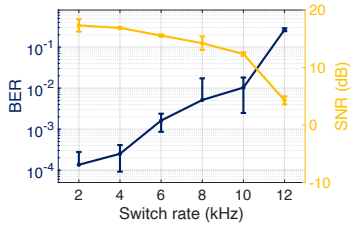


**Figure 22: Impact of switch rate.**

QPSK codebooks against randomly generated ones. The experiment was conducted at three reader-to-tag distances: 5 m, 10 m, and 20 m. At each distance, we generated 10 random QPSK codebooks and compared BER. Figure 17 presents the result. While random codebooks are capable of achieving a low BER at 5 m, their performance deteriorates sharply as the range extends to 10 m and 20 m. In contrast, our optimized codebook maintains a robust and stable medium BER around $10^{-4}$ and $3.75 \times 10^{-4}$, respectively. This superior performance stems from our optimization process, designed to simultaneously maximize the backscatter signal power and the phase separation between constellation points.

**Performance across Different Hydrophone Channels.** In this section, we would like to quantify the impact of the number of hydrophone channels at the receiver on the BER performance. To this end, we used the same QPSK received signals from Section 6.1 but processed the data by varying the number of hydrophone channels. Specifically, for each trial, we used a multichannel DFE decoder but applied it to a different number of hydrophone channels. For completeness, we used every possible combination of $N = 2, 4, 6, 8$ hydrophone channels in generating these results. Specifically, for any number of selected receive channels N, we generate $C_8^N$ unique combinations of receive channels to use in the decoding pipeline and compute CDFs of these selected combinations. As shown in Figure 18, MetaScatter's median and 90% BER decrease from $2 \times 10^{-2}$ and 0.5 to $10^{-4}$ and $10^{-2}$, respectively, as the hydrophone channels increases from 2 to 8. This is because multiple channels provide gains in received power and spatial diversity. Additionally, the system maintains a BER of about $10^{-3}$ in 80% of the cases when using an 8-channel hydrophone array, demonstrating the robustness of MetaScatter's decoding capability.

**Performance across Different Metasurface Sizes.** We further evaluated how MetaScatter's gain varies with its physical size. In the experiment, we fixed the distance between the reader and metasurface as 10 m and compared the SNR and BER performance of metasurfaces sized $7 \times 7$ ($16.8\ cm \times 16.8\ cm$), $7 \times 14$ ($16.8\ cm \times 33.6\ cm$), and $14 \times 14$ ($33.6\ cm \times 33.6\ cm$). As shown in Figure 19, increasing the metasurface size from $7 \times 7$ to $7 \times 14$ and then to $14 \times 14$ raises the median SNR from 10 dB to 15 dB and 22 dB, respectively. The increasing trend in SNR is expected, as adding more meta-atoms to the metasurface array increases its gain, which in turn improves the SNR. Similarly, the median BER decreases from $10^{-2}$ to $10^{-3}$ and then to $10^{-4}$ as the metasurface size increases due to the SNR improvement.

## 6.3 Factors Affecting Performance

**Performance under Different Dynamic Interference.** In this section, we evaluate the performance of MetaScatter under varying levels of dynamic interference—namely, quiet, noisy, and busy conditions. The experiment setup is shown in Figure 20 (left), where the reader-metasurface distance is set to be 10 m. The noisy (R1&R2) and busy conditions (R3) are created by volunteers swimming either near (R2) to or far (R1) from the link path, or repeatedly crossing it (R3), thereby generating time-varying multipath reflections and surface-wave turbulence that progressively degrade channel quality. As shown in Figure 20 (right), the BER slightly increases in the presence of such interference. The BER at location R3 is slightly higher than those at other locations. Nevertheless, the averaged BER remains below $2 \times 10^{-3}$, demonstrating

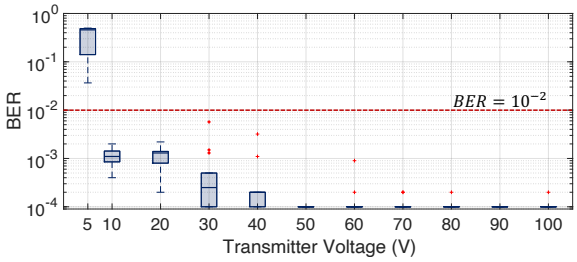


**Figure 23: Impact of different transmitter voltages.**

MetaScatter's robustness against interference. This resilience stems from MetaScatter's beamforming capability and its multi-channel DEF algorithm, which jointly provide the high SNR needed for high-order modulation.

**Performance across Different Angles.** We consider the retro-reflection scenario, in which the incident signal is reflected back toward the source, to evaluate the beam-steering capability. We configure MetaScatter to operate in retro-reflective mode for incident angles ranging from 10° to 50° relative to broadside. Figure 21 compares the BER and SNR at the main lobe and at the specular-reflection direction. As the reflection angle increases, the retro-reflected SNR gradually decreases, mainly owing to the limited field of view (FoV) of the metasurface. Nevertheless, the averaged BER remains below $10^{-3}$, and the effective FoV of MetaScatter is approximately ±50°.

**Performance across Different Backscatter Switch Rates.** To evaluate MetaScatter's ability to communicate across different bitrates, we fixed the distance between the reader and the metasurface at 10 m and varied the backscatter switch rate. In each experimental trial, we repeated the measurement five times. The hydrophone received the backscatter node's packets and computed the BER and SNR of the received signals. As shown in Figure 22, the SNR decreased and the BER increased with higher switch rates, because the fixed transmit power was spread over a proportionally wider bandwidth, reducing the energy per symbol. Nevertheless, MetaScatter achieved reliable QPSK decoding at a switch rate of about 10 kHz.

**Performance across Different Transmitter Voltages.** Next, we evaluate the impact of the reader's transmit power on MetaScatter. Although the MetaScatter backscatter node consumes a constant amount of power, the overall system performance still depends on the transmit power of the reader. Since higher transmit power leads to stronger backscattered signals, we expect a higher SNR at the receiver and, consequently, improved BER performance. We fixed the distance between the reader and metasurface at 10 m and compared the BER performance of QPSK under different transmit power levels. Here, we applied an input voltage of 5–100 V to drive the 200 Ω transducer, which is consistent with prior work [24]. At each transmitter voltage level, we conducted five trials at a data rate of 1000 bps. Figure 23 shows the median BER as a function of transmitter voltage. As the transmitter voltage increases, the BER consistently improves. When the transmitter voltage exceeds 10 V, the BER falls below $10^{-2}$, and at 50 V, the median BER reaches approximately $10^{-4}$. These results highlight MetaScatter's ability to achieve reliable performance even at low transmitter voltages, owing to its high gain.

**Table 1: Power consumption of MetaScatter.**

| Components | Idle Power (mW) | Active Power (mW) |
|---|---|---|
| MCU | 0.18 | 0.92 |
| Switches | / | 0.196 |
| Total | 0.18 | 1.116 |

## 6.4 Power Consumption

In this section, we evaluate the power consumption of MetaScatter's backscatter tag. We used a Monsoon power monitor (AAA10F [33]) to measure the power consumption. Table 1 presents the measured power when the MetaScatter tag is in idle state (waiting to receive a downlink signal) as well as when it is backscattering. Each state's measurement includes the power consumption of the MCU and electronic switches. The table shows that the power consumption in idle state is 0.18 $mW$ and increases to around 1.116 $mW$ for the backscattering state. We note that the core component of our electronic switch implementation (i.e., the TMUX1134PWR switches) consumes only 4 $\mu W$ for each 4-channel switch when modulating the backscatter signal at a 1 $kHz$ rate, which aligns with the prior works [18, 24]. The total power consumption of the active mode is slightly higher than existing underwater backscatter technologies. This is because MetaScatter's MCU requires additional pins and switches to control the metasurface for beamforming. Nevertheless, the overall power consumption remains around 1 mW, which is much lower than that of active transmission.

# 7 Related Work

**Acoustic Backscatter.** Acoustic backscatter [19, 24, 38] is an emerging ultra-low-power communication technique designed for scenarios in which electromagnetic waves are ineffective. For example, previous studies have investigated the use of backscatter in underwater environments to support a range of applications. PAB [24] designed a backscatter node capable of measuring parameters such as pH, temperature, and pressure. SeaScan [35] and a recent study [2] proposed systems for marine imaging, while VAB [14] employed a Van Atta structure in underwater backscatter to enable long-range communication. However, these solutions still rely on binary modulation, resulting in low data rates. To improve throughput, U2B [18] proposed an ultra-wideband

underwater backscatter using piezoelectric metamaterials. MetaScatter complements this wideband design by improving spectrum utilization with high-order modulation.

**High-order Acoustic Backscatter Communication.** High-order modulation schemes have been demonstrated to increase data rates in existing wireless communication systems. Some works [3, 38] introduced high-order acoustic backscatter modulation by toggling between multiple impedance states. Despite these advancements, state-of-the-art underwater backscatter systems remain limited to four reflection states (i.e., QPSK) and achieve only a short communication range. The fundamental bottleneck is that existing tags rely on an omnidirectional PZT cylinder, which reflects signals in all directions. This spherical power spreading leads to power loss and substantially degrades the received SNR. Increasing the number of reflection states further exacerbates the problem, as the reduced symbol spacing makes the system even more sensitive to SNR degradation. In contrast, MetaScatter introduces both hardware and software designs to enable simultaneous beamforming and high-order modulation. For QPSK, MetaScatter achieves a round-trip communication range of 60 m, significantly exceeding the 10 m range reported in existing work [3]. Moreover, our system supports higher-order modulations such as 8-QAM and 16-QAM.

**RF-based Metasurface Modulation.** Numerous metasurfaces operating in the radio signal frequency (RF) band have been proposed [12, 15, 22, 27, 29, 32, 39, 43, 49]. By controlling the phase configuration (i.e., codebook) of each meta-atom, metasurfaces can modulate data onto the incident carrier wave [12, 22]. However, acoustic signals are mechanical waves, and existing RF metasurface hardware designs cannot be directly applied to them. Furthermore, existing RF metasurfaces typically rely on spatio-temporal modulation [12, 22], which incurs high computational complexity. Some designs [12] mitigate this burden using continuously tunable phase. However, achieving continuously tunable phase in acoustic metasurfaces is challenging, as components commonly used in RF systems, such as varactor diodes, are not available in acoustic systems. In contrast, MetaScatter shows that for typical metasurfaces with tens of meta-atoms or more, even a simple 1-bit metasurface is sufficient to enable both effective beamforming and high-order modulation. The resulting search space of $O(2^{N\times N})$ is further reduced to $O(LNN)$ in our system.

**Acoustic Metasurface.** Acoustic metasurfaces are structures capable of manipulating the propagation of acoustic waves, including their reflection [21], transmission [16, 17, 55], and absorption [52]. Previous studies [16, 17, 21, 48, 51, 54, 55] have demonstrated that deploying metasurfaces can create an intelligent environment to strengthen wireless communication and sensing links. Most of these studies [16, 17, 55] rely on passive structures, such as Helmholtz resonators. Some other metasurfaces use mechanical structures [21] or emerging materials [48, 54] that are controlled by slow mechanical movements or power-hungry magnetic fields. The most closely related work involves piezoelectric materials to enable PZT-metasurface [40]. However, existing PZT-metasurface designed for in-air operation exhibit a small impedance difference from water, leading to efficiency loss and fundamentally limiting their underwater applicability. To overcome this, we leverage a shell coupled to the piezoelectric meta-atom and optimize its geometry and material to enhance its acoustic impedance, thereby improving the overall reflection efficiency. We also provide a detailed fabrication workflow and waterproofing scheme to facilitate underwater experiments for the research community.

## 8 Discussion

**Supporting Higher-order Modulation Schemes.** The current implementation of MetaScatter supports up to 16-QAM. Scaling to higher orders is challenging, as constellation points become less separable and demand higher SNR for reliable decoding.A promising approach is to increase the metasurface size to enhance beamforming gain, thereby supporting even higher-order modulations.

**Device Mobility.** The current design of MetaScatter primarily targets stationary deployments, which are typical in coastal monitoring and other low-mobility environments. In mobile scenarios, however, MetaScatter would need to incorporate beam steering to continuously track and align with the receiver's main lobe. As future work, we plan to extend MetaScatter to support mobility, enabling applications on underwater drones and surface vessels.

## 9 Conclusion

We present MetaScatter, a low-power, metasurface-based underwater backscatter system that enables high-order modulation and passive beamforming for underwater communication. By intelligently controlling the signal phase, MetaScatter simultaneously achieves beamforming and high-order modulation. Real-world experiments demonstrate robust links, with significant improvements in throughput and range over state-of-the-art systems. These results highlight the potential of metasurface-assisted backscatter as a foundation for scalable, energy-efficient underwater IoT.

## 10 ACKNOWLEDGMENTS

This work is supported by the National Natural Science Foundation of China under Grants (62572395, 62372374, 62502384) and the Key Research and Development Program of Shaanxi under Grants (2024GH-ZDXM-46 and 2024GH-ZDXM-49). We thank the anonymous reviewers and the shepherd for their valuable feedback.

## References


[1] COMSOL Multiphysics 6.0. Simulate real-world designs, devices, and processes with multiphysics software from comsol., 2022.

[2] Sayed Saad Afzal, Waleed Akbar, Osvy Rodriguez, Mario Doumet, Unsoo Ha, Reza Ghaffarivardavagh, and Fadel Adib. Battery-free wireless imaging of underwater environments. *Nature communications*, 13(1):5546, 2022.

[3] Sayed Saad Afzal, Reza Ghaffarivardavagh, Waleed Akbar, Osvy Rodriguez, and Fadel Adib. Enabling higher-order modulation for underwater backscatter communication. In *Global Oceans 2020: Singapore–US Gulf Coast*, pages 1–6. IEEE, 2020.

[4] Aigtek Co., Ltd. ATA-214 high voltage amplifier. https://www.aigtek.cn/products/108.html, 2024. Accessed: 2024-05-07.

[5] Waleed Akbar, Ahmed Allam, and Fadel Adib. The underwater backscatter channel: Theory, link budget, and experimental validation. In *Proceedings of the 29th Annual International Conference on Mobile Computing and Networking*, pages 1–15, 2023.

[6] Shujaat Ali, Muhammad Nadeem, Sheeraz Ahmed, and Muhamad Tahir. Iot-based framework for optimizing energy efficiency and reliability in acoustic sensor networks using mobile sinks. *Scientific Reports*, 14(1):24122, 2024.

[7] Alibaba.com. Piezo ceramic plate type PZT-5H piezoelectric crystal ultrasonic transducer used for medical scalpel. https://www.alibaba.com/product-detail/Piezo-ceramic-plate-type-PZT-5H_60699905376.html, 2024. Accessed: 2024-05-07.

[8] Aquarian Audio Products. H1a hydrophone. https://www.aquarianaudio.com/h1a-hydrophone.html, 2024. Accessed: 2024-05-07.

[9] Aquarian Audio Products. PA6 phantom-powered hydrophone preamp. https://www.aquarianaudio.com/pa6.html, 2024. Accessed: 2024-05-07.

[10] Beijing Tonglian Hengxing Technology Co., Ltd. Goet-1080 epoxy ab mixture. https://e.tb.cn/h.hD0utETQelfenEX?tk=wvj34NjskWt.

[11] Dinesh Bharadia, Kiran Raj Joshi, Manikanta Kotaru, and Sachin Katti. Backfi: High throughput wifi backscatter. *ACM SIGCOMM Computer Communication Review*, 45(4):283–296, 2015.

[12] Jun Yan Dai, Wankai Tang, Liu Xi Yang, Xiang Li, Ming Zheng Chen, Jun Chen Ke, Qiang Cheng, Shi Jin, and Tie Jun Cui. Realization of multi-modulation schemes for wireless communication by time-domain digital coding metasurface. *IEEE transactions on antennas and propagation*, 68(3):1618–1627, 2019.

[13] Caihui Du, Jihong Yu, Rongrong Zhang, Ju Ren, and Jianping An. Orthcatter: High-throughput in-band {OFDM} backscatter with {Over-the-Air} code division. In *21st USENIX Symposium on Networked Systems Design and Implementation (NSDI 24)*, pages 1301–1314, 2024.

[14] Aline Eid, Jack Rademacher, Waleed Akbar, Purui Wang, Ahmed Allam, and Fadel Adib. Enabling long-range underwater backscatter via van atta acoustic networks. In *Proceedings of the ACM SIGCOMM 2023 Conference*, pages 1–19, 2023.

[15] Chao Feng, Xinyi Li, Yangfan Zhang, Xiaojing Wang, Liqiong Chang, Fuwei Wang, Xinyu Zhang, and Xiaojiang Chen. Rflens: metasurface-enabled beamforming for iot communication and sensing. In *Proceedings of the 27th Annual International Conference on Mobile Computing and Networking*, pages 587–600, 2021.

[16] Yongjian Fu, Yongzhao Zhang, Yu Lu, Lili Qiu, Yi-Chao Chen, Yezhou Wang, Mei Wang, Yijie Li, Ju Ren, and Yaoxue Zhang. Adaptive metasurface-based acoustic imaging using joint optimization. In *Proceedings of the 22nd Annual International Conference on Mobile Systems, Applications and Services*, pages 492–504, 2024.

[17] Yongjian Fu, Yongzhao Zhang, Hao Pan, Yu Lu, Xinyi Li, Lili Chen, Ju Ren, Xiong Li, Xiaosong Zhang, and Yaoxue Zhang. Pushing the limits of acoustic spatial perception via incident angle encoding. *Proceedings of the ACM on Interactive, Mobile, Wearable and Ubiquitous Technologies*, 8(2):1–28, 2024.

[18] Reza Ghaffarivardavagh, Sayed Saad Afzal, Osvy Rodriguez, and Fadel Adib. Ultra-wideband underwater backscatter via piezoelectric metamaterials. In *Proceedings of the Annual conference of the ACM Special Interest Group on Data Communication on the applications, technologies, architectures, and protocols for computer communication*, pages 722–734, 2020.

[19] Zheng Gong, Lubing Han, Zhenlin An, Lei Yang, Siqi Ding, and Yu Xiang. Empowering smart buildings with self-sensing concrete for structural health monitoring. In *Proceedings of the ACM SIGCOMM 2022 Conference*, pages 560–575, 2022.

[20] Xiuzhen Guo, Yuan He, Zihao Yu, Jiacheng Zhang, Yunhao Liu, and Longfei Shangguan. Rf-transformer: A unified backscatter radio hardware abstraction. In *Proceedings of the 28th annual international conference on mobile computing and networking*, pages 446–458, 2022.

[21] Juan He, Jie Xiong, Weihang Hu, Chao Feng, Enjie Yao, Xiaojing Wang, Chen Liu, and Xiaojiang Chen. Cw-acouslen: a configurable wideband acoustic metasurface. In *Proceedings of the 22nd Annual International Conference on Mobile Systems, Applications and Services*, pages 29–41, 2024.

[22] John A Hodge, Kumar Vijay Mishra, and Amir I Zaghloul. Intelligent time-varying metasurface transceiver for index modulation in 6g wireless networks. *IEEE Antennas and Wireless Propagation Letters*, 19(11):1891–1895, 2020.

[23] John H Holland. Genetic algorithms. *Scientific american*, 267(1):66–73, 1992.

[24] Junsu Jang and Fadel Adib. Underwater backscatter networking. In *Proceedings of the ACM special interest group on data communication*, pages 187–199. 2019.

[25] James Kennedy and Russell Eberhart. Particle swarm optimization. In *Proceedings of ICNN'95-international conference on neural networks*, volume 4, pages 1942–1948. IEEE, 1995.

[26] Delphin Raj Kesari Mary, Eunbi Ko, Dong Jin Yoon, Soo-Young Shin, and Soo-Hyun Park. Energy optimization techniques in underwater internet of things: issues, state-of-the-art, and future directions. *Water*, 14(20):3240, 2022.

[27] Minseok Kim, Namjo Ahn, and Song Min Kim. Nr-surface: Nextg-ready $\mu$w-reconfigurable mmwave metasurface. In *NSDI*, 2024.

[28] LCSC Electronics. Magnetic Shielded Inductor. Product Page, 2025. Accessed: 2025-08-19.

[29] Xinyi Li, Chao Feng, Xiaojing Wang, Yangfan Zhang, Yaxiong Xie, and Xiaojiang Chen. {RF-Bouncer}: A programmable dual-band metasurface for sub-6 wireless networks. In *20th USENIX Symposium on Networked Systems Design and Implementation (NSDI 23)*, pages 389–404, 2023.

[30] Chi Lin, Jianan Lin, Jie Xiong, Qiwei Wang, Lei Wang, Guowei Wu, Xin Fan, and Zhongxuan Luo. Uwbeacon: Lighting up centimeter-level underwater positioning. In *Proceedings of the 30th Annual International Conference on Mobile Computing and Networking*, pages 1222–1236, 2024.

[31] Guancong Ma, Xiying Fan, Ping Sheng, and Mathias Fink. Shaping reverberating sound fields with an actively tunable metasurface. *Proceedings of the National Academy of Sciences*, 115(26):6638–6643, 2018.

[32] Ruichun Ma, Shicheng Zheng, Hao Pan, Lili Qiu, Xingyu Chen, Liangyu Liu, Yihong Liu, Wenjun Hu, and Ju Ren. Automs: Automated service for mmwave coverage optimization using low-cost metasurfaces. In *Proceedings of the 30th Annual International Conference on Mobile Computing and Networking*, pages 62–76, 2024.

[33] Monsoon Solutions. High voltage power monitor part number: Aaa10f. https://www.msoon.com/hvpm-product-documentation, 2025. Accessed: 2025-08-24.

[34] Xin Na, Xiuzhen Guo, Zihao Yu, Jia Zhang, Yuan He, and Yunhao Liu. Leggiero: Analog wifi backscatter with payload transparency. In *Proceedings of the 21st Annual International Conference on Mobile Systems, Applications and Services*, pages 436–449, 2023.

[35] Nazish Naeem, Jack Rademacher, Ritik Patnaik, Tara Boroushaki, and Fadel Adib. Seascan: An energy-efficient underwater camera for wireless 3d color imaging. In *Proceedings of the 30th Annual International Conference on Mobile Computing and Networking*, pages 785–799, 2024.

[36] National Oceanic and Atmospheric Administration. Ocean exploration matters. https://oceanexplorer.noaa.gov/why-exploration-matters/why-exploration-matters.html, 2024. Accessed: 2025-09-03.

[37] NCEAS. Ocean vital signs are stable, but bill of health isn't clean, 2025.

[38] Peter Oppermann and Christian Renner. Higher-order modulation for acoustic backscatter communication in metals. In *Proceedings of the ACM SIGCOMM 2022 Conference*, pages 576–587, 2022.

[39] Hao Pan, Lili Qiu, Bei Ouyang, Shicheng Zheng, Yongzhao Zhang, Yi-Chao Chen, and Guangtao Xue. Pmsat: Optimizing passive metasurface for low earth orbit satellite communication. In *Proceedings of the 29th Annual International Conference on Mobile Computing and Networking*, pages 1–15, 2023.

[40] Yao-Yin Peng, Zhang-Zhao Yang, Zhi-Lei Zhang, Xin-Ye Zou, Chao Tao, and Jian-Chun Cheng. Tunable acoustic metasurface based on tunable piezoelectric composite structure. *The Journal of the Acoustical Society of America*, 151(2):838–845, 2022.

[41] Qihui Qin, Kai Chen, Yaxiong Xie, Heng Luo, Dingyi Fang, and Xiaojiang Chen. Pushing the throughput limit of ofdm-based wi-fi backscatter communication. In *Proceedings of the 30th Annual International Conference on Mobile Computing and Networking*, pages 968–983, 2024.

[42] RIGOL Technologies Inc. DG1022 arbitrary waveform function generator. https://www.rigolna.com/products/waveform-generators/dg1000/dg1022/products/, 2024. Accessed: 2024-05-07.

[43] Yiwen Song, Hao Pan, Longyuan Ge, Lili Qiu, Swarun Kumar, and Yi-Chao Chen. Microsurf: Guiding energy distribution inside microwave oven with metasurfaces. In *Proceedings of the 30th Annual International Conference on Mobile Computing and Networking*, pages 1346–1360, 2024.

[44] Milica Stojanovic, Josko Catipovic, and John G Proakis. Adaptive multichannel combining and equalization for underwater acoustic communications. *The Journal of the Acoustical Society of America*, 94(3):1621–1631, 1993.

[45] Texas Instruments. MSP430G2553 16 MHz MCU with 16 KB Flash, 512 B SRAM. Product Page, 2025. Accessed: 2025-08-18.

[46] Texas Instruments. TS5A23166. Product Page, 2025. Accessed: 2025-08-18.

[47] Stewart Thomas and Matthew S Reynolds. Qam backscatter for passive uhf rfid tags. In *2010 IEEE International Conference on RFID (IEEE RFID 2010)*, pages 210–214. IEEE, 2010.

[48] Qiyuan Wang, Philipp del Hougne, and Guancong Ma. Controlling the spatiotemporal response of transient reverberating sound. *Physical Review Applied*, 17(4):044007, 2022.

[49] Yezhou Wang, Hao Pan, Lili Qiu, Linghui Zhong, Jiting Liu, Ruichun Ma, Yi-Chao Chen, Guangtao Xue, and Ju Ren. Gpms: Enabling indoor gnss positioning using passive metasurfaces. In *Proceedings of the 30th Annual International Conference on Mobile Computing and Networking*, pages 1424–1438, 2024.

[50] Wayne Kerr Electronics. 6500B series precision impedance analyzer. https://www.waynekerrtest.com/products_detail.php?indexs=4, 2024. Accessed: 2024-05-07.

[51] Kai Wu, Jing-Jing Liu, Yu-jiang Ding, Wei Wang, Bin Liang, and Jian-Chun Cheng. Metamaterial-based real-time communication with high information density by multipath twisting of acoustic wave. *Nature communications*, 13(1):5171, 2022.

[52] Jieun Yang, Joong Seok Lee, and Yoon Young Kim. Multiple slow waves in metaporous layers for broadband sound absorption. *Journal of Physics D: Applied Physics*, 50(1):015301, 2016.

[53] ZDYW-28K-S-Transducer. Product page. https://e.tb.cn/h.hwtvPhHsVBKldCx?tk=s3sm4NQl8lc.

[54] Hongkuan Zhang, Qiyuan Wang, Mathias Fink, and Guancong Ma. Optimizing multi-user indoor sound communications with acoustic reconfigurable metasurfaces. *Nature Communications*, 15(1):1270, 2024.

[55] Yongzhao Zhang, Yezhou Wang, Lanqing Yang, Mei Wang, Yi-Chao Chen, Lili Qiu, Yihong Liu, Guangtao Xue, and Jiadi Yu. Acoustic sensing and communication using metasurface. In *20th USENIX Symposium on Networked Systems Design and Implementation (NSDI 23)*, pages 1359–1374, 2023.

[56] Zheng Zhang, Yu Rou Jia, Wei Xiang Jiang, Xin Ge Zhang, Cheng-Wei Qiu, and Tie Jun Cui. Programming reflected and transmitted sound behaviors based on motor-driven digital metasurface. *Advanced Functional Materials*, 34(48):2411403, 2024.

[57] Zoom Corporation. F8n Pro 8-channel field recorder. https://www.bhphotovideo.com/c/product/1692954-REG/zoom_zf8npro_8_channel_field_recorder_with.html, 2024. Accessed: 2025-05-06.

# A APPENDIX

**Table 2: Parameters of the meta-atom.**

| Parameter | Value (mm) | Parameter | Value (mm) |
|---|---|---|---|
| D | 24 | $h_1$ | 1 |
| r | 7 | $h_2$ | 1 |
| t | 4 | $h_3$ | 1 |
| L | 5 | $h_4$ | 3 |
| $d_1$ | 15 | $l_1$ | 10 |
| $d_2$ | 22 | $l_2$ | 9 |